JOURNAL OF MATERIALS SCIENCE **38** (2003) 747 – 757

Cavitation damage to geomaterials in a flowing system

A. W. MOMBER
RWTH Aachen, Dept. of Mining, Metallurgy and Geoscience, Lochnerstr, 4-20, D-52064 Aachen Germany

Short-time cavitation erosion of rocks and cementitious composites is investigated in a laboratory flow cavitation chamber. Cavitation erosion with an exposure time as low as 10 seconds generates measurable damage. Mineral composition plays a major role in the cavitation erosion of the material. The erosion mainly occurs in an intergranular or intercrystalline mode, respectively. Fracture toughness of rock and conventional concrete is a good indication of cavitation erosion resistance. However, density is a second important evaluation parameter; materials with a low degree of pre-existing flaws, namely glass and high-strength silica cement, show an extraordinary high erosion resistance. The cavitation erosion of the rock materials tested in this study is always higher than that of conventional concrete mixtures. Elastic strain energy density is not a measure of cavitation erosion resistance of rocks and cementitious composites. A parameter $\Phi = d_M \cdot E_M \cdot \rho_M / K_{Ic}^n$ is derived to approximate the cavitation erosion resistance of the materials. The parameter n is a function of the R-curve-behavior.

1. Introduction

Cavitation erosion of rocks is of interest to engineers and researchers for several reasons. Firstly, flow cavitation in hydraulic structures is a severe economic problem in hydraulic engineering. Many hydraulic structures, such as canals, river linings, and flow channels, are made from rock materials. Ribeiro *et al.* [1] reported that the eroded volume, accumulated over a period of only 5 years, in a granite river bed is as high as 38,400 m^3. Secondly, melted glacial water or water from melted snow flowing with a high speed over rock surfaces causes severe erosion due to flow cavitation [2]. Thirdly, cavitation erosion can be used to assist rock drilling. Early attempts to utilise cavitation erosion as a rock drilling method are reported in [3] and [4]. Later, Mazurkiewicz and Summers [5] performed preliminary studies about the selective disintegration of ore in a cavitation cell. Cavitation erosion, as an additional failure mechanism, seems also to be very likely in drop impact and fluid jet erosion processes [6].

Systematic investigations about the microscopic failure of rocks during cavitation erosion are quite rare. Erdmann-Jesnitzer *et al.* [7] investigated the behaviour of diabase and granite. Diabas showed a rather low cavitation erosion resistance compared to granite. In the latter material, a net of microcracks was formed, but the cracks very often did not intersect. Mazurkiewicz and Summers [5] noted on dolomite samples that micropores are the origin of microcrack formation; material was removed due to the intersection of individual cracks. The cavitation erosion of concrete materials is recently reviewed in [8].

Short-time cavitation erosion—defined here as cavitation with an exposure time of up to $t_E = 180$ s—is a promising method to study the material removal mechanisms acting in the early stage of cavitation erosion. Cavitation is the growth and implosion of gas bubbles in a fluid. Basically, flow cavitation and acoustically induced cavitation can be distinguished, whereas the first type is more common in practice and is, therefore, used in this study. Detailed descriptions of cavitation phenomena are provided in the standard literature [9–11]. Cavitation can damage and erode materials by the following mechanisms: generation of shock waves due to symmetric bubble implosion; formation of microjets due to non-symmetric bubble implosion [12]; collapse of bubble clusters [13]. However, a superposition of several individual mechanisms is very likely. The pressure generated during the implosion and collapse of cavitation bubbles is typically in the range of several 10^2 MPa [10]. More recently, a splash effect with follows the impact of the liquid jet and produces a double pressure peak is proposed [14].

2. Materials and experimental set-up

2.1. Material properties

For the key experiments, six different materials were used: four rock materials and two conventional concrete materials. The properties of these materials are listed in Table I. However, additional tests were performed with a marble, a high-strength silica cement, a mortar, a hardened cement paste, and a glass sample. The two conventional concrete materials, concrete 45

TABLE I Properties of the investigated materials

Material	Splitting strength (MPa)	Density (kg/m^3)	Fracture toughness (MNm$^{-3/2}$)	Maximum grain size (mm)	Compressive strength (MPa)	Young's modulus (GPa)
Concrete 25	–	2150	0.40	16	23	–
Concrete 35	–	2340	0.67	16	36	–
Concrete 45	3.4	1990	0.31	5	50	37
Concrete 55	3.9	2190	0.49	16	60	39
Glass	–	2200	0.70	–	–	–
Granite	10.7	2500	0.80	–	160	52.4
Limestone	10.7	2500	1.21	5	55	82
Marble	21	2670	1.50	–	130	–
Rhyolite	12.2	2700	1.17	13	240	45
Shale	–	2600	2.70	0.2	150	–
Silica cement	–	1750	0.55	–	80	–

and concrete 55, are manufactured according to the German DIN 1048. The cement used was a Portland-cement type PZ 45 F; the water-cement-ratio was 0.5 for the concrete 45, and 0.4 for the concrete 55. The coarse aggregate used was a gravel consisting of pure silica and quartz, and the fine aggregate was a rounded quartz sand. Concrete 45 was rather a fine-grained concrete with a maximum aggregate size $d_M = 5$ mm, whereas the concrete 55 was a coarse material with a maximum aggregate size $d_M = 16$ mm. The silica cement did not contain sand or aggregate; it was a mixture of hardened cement paste and fine silica dust that guarantees a very dense structure. The concrete samples 25 and 35 were commercial mixtures. The granite was a Portuguese granite with a crystalline structure. The rock forming minerals are mica (black), quartz (white) and feldspar (dark grey). The structure was dense. The bond forces between the individual minerals was higher than the cohesion forces in the minerals. Therefore, the fracture behaviour is dominated by the cleavage of the minerals. Due to the tectonic loading, a pronounced pre-existing microcrack net was formed in the material. The porphyry was a porphyric rhyolite consisting of a matrix (approximately 50 volume-percent) and embedded coarse particles. Major mineral components were potassium feldspar (pink), sodium feldspar (white) and quartz (dark). The non-crystalline matrix was dense and fine-grained (average matrix particle size about 0.1 mm). The inclusions had a maximum grain size of about 13 mm. The limestone was a sedimentary Jurassic limestone consisting of a fine-grained matrix with an average grain size in the 1/10-mm-range and embedded broken shells. These organic inclusions may lead to local strength reduction. However, the calcitic matrix was very dense. The shale was a German clay schist with a layered structure. The layers could be identified as a white, quartz-rich paleband, and a dark band containing a high amount of mud and organic substances. The layer thickness was between 4 mm and 6 mm. Pronounced cleavage could be noticed as the specimens were loaded parallel to the layers. The properties listed in Table I are estimated perpendicular to the layer structure. The marble was a conventional Tassos marble consisting mainly of calcite and graphite; the structure was not reviewed.

The fracture toughness values listed in Table I were estimated on a single edge cracked three point bending specimen according to the procedure described in [15].

2.2. Experimental set-up

The cavitation erosion experiments were run in the flow system shown in Fig. 1. The flow chamber basically consists of a water flow inlet, an outlet, weir, counter-weir, and specimen fixture. For all tests, the cavitation number was kept at a level of $\sigma_C = 0.075$. Cavitation number for the flow system can be estimated as follows:

$$\sigma_C = \frac{2 \cdot (p_2 - p_V)}{\rho_F \cdot v_F}, \tag{1}$$

where p_2 is the pressure after the weir, p_V is the vapour pressure, ρ_F is the fluid density, and v_F is the flow velocity. The water temperature in the cavitation chamber

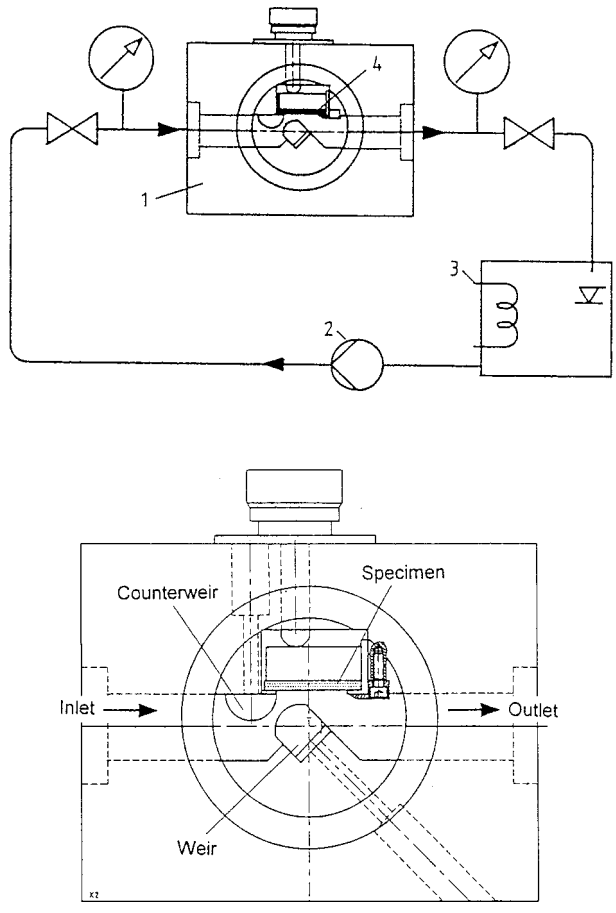

Figure 1 Experimental set-up, 1: Flow chamber, 2: Pump, 3: Cooling system, 4: Specimen.

was 40°C, the pH-value of the water was 8, and the oxygen content of the water was 5 pmm. The pressure before the weir was 1.1 MPa, and the pressure after the weir was 0.17 MPa. The cavitation conditions were calibrated through a test on a standard aluminium sample. The exposure time was between $t_E = 5$ s and $t_E = 180$ s. Three specimens of each mixture were tested for every experimental condition. These specimens were cut away from large samples by a diamond saw and had the following dimensions: 6 cm in length, 3 cm in width, and 1 cm in height (which is the dimension shown in Fig. 1). After the cavitation erosion tests, the mass loss was estimated by a precision balance type 'Mettler Toledo AB 204' with a maximum capacity of 210 g and an accuracy of ± 50 μg. The mass loss was measured prior to the cavitation (m_1) and after cavitation (m_2). In order to exclude the mass of permeating water flow into the porous material during the cavitation test, each specimen was dried after the cavitation test in an electric oven. The erosion rate was estimated as follows:

$$E_R = \frac{m_1 - m_2}{t_C}. \tag{2}$$

The unit of the cavitation erosion rate is mg/s. Microscopic inspections of the erosion sites were performed with an optical microscope with magnifications up to 80×.

3. Experimental results and discussion

3.1. Structure and basic dimensions of erosion sites

Two sections of different cavitation erosion intensity were identified at the specimen surfaces: a section with high intensity in the central region (referred to as zone I) and a section of low intensity at the periphery (referred to as zone II). These two zones, however, are a result of the flow conditions in the cavitation chamber [16]. They were already noted in a previous study [8]. The situation is illustrated in Fig. 2 based on erosion sites in a glass sample. Fig. 2a shows the situation in zone I: this zone is severely damaged through intense cavitation. The dimension of the zone I depends on material properties and exposure time. Fig. 2b shows a transition range. This transition from an accumulation of several small individual erosion tips to a single large cavity could be observed in the rocks and cementitious materials at a certain threshold exposure time. This critical exposure time is ca. 50 s for rhyolite, 30 s for marble, 90 s for limestone, 60 s for schist, less than 60 s for granite, and less than 5 s for the concrete mixtures. If the exposure time increases further, the zone-I-cavities expand. For the concrete mixtures the dimension of zone I is almost one order of magnitude larger than for the rock materials. The structure of zone II was best visible at the glass surfaces and at the surfaces of large individual grains in the other materials. Example are shown in Figs 2c and 3 (note the short exposure time for Fig. 3). Typical dimensions of these impressions are 100 μm to 200 μm in glass, 400 μm in concrete aggregate, and 800 μm in rhyolite.

If the formation of a microjet due to asymmetric bubble implosion is assumed to be the primary erosion mode it may be of interest to compare jet diameter and pit dimension in zone II. The diameter of a microjet can be approximated as follows [17]:

$$d_J \cong 0.1 \cdot R_O, \tag{3}$$

where R_O is the radius of the bubble before the collapse. The radius of the bubble before the collapse is about $R_O = 100$ μm for the conditions in the cavitation chamber [18]. Therefore, the microjet diameter is $d_J = 10$ μm which is an order of magnitude lower than the pit diameters. The duration of the stress pulse generated during microjet impact can be evaluated using the following equation [19]:

$$t_P = \frac{d_J}{2 \cdot c_W}. \tag{4}$$

In this equation, c_W is the shock wave speed in the fluid: $c_W = c_0 + 2 \cdot v_J$. With $c_0 = 1460$ m/s (sound of speed in water) and $v_J = 500$ m/s (average value from measurements performed on collapsing cavitation bubbles in [20]), the stress pulse duration is $t_P = 2 \cdot 10^{-9}$ s. Considering a crack velocity of 1270 m/s for a marble measured during contact detonation [21], the length of a crack formed during the collapse of a single cavitation bubble is as short as $L = 2.5$ μm. This value is two orders of magnitude lower than typical pit sizes observed in the materials, and multiple microjet impact may be required to form the pits in zone II. However, quite different results occur if splash effects are considered as described in [14]. The duration of double-peaks was found to last over a period in the μs-range which delivers crack lengths of about 2 mm. Interestingly, this value is in the order of the perimeter of some of the formed pits.

3.2. Microscopic material erosion modes

In the rhyolite samples, matrix and inclusions are eroded simultaneously, but matrix material is damaged more severely (see Fig. 4a). The matrix fails in a rather intergranular mode; the exposed grains have diameters between 40 μm and 100 μm. In the quartz inclusions, conchoidal fractures were formed (very similar to those observed in the glass sample); a typical fracture dimension is 120 μm. Sodium feldspar inclusions are broken in a layer-by-layer mode, showing pronounced cleavage planes formed through transcrystalline fracture; this is illustrated in Fig. 4b. Potassium feldspar fails by intergranular crystal separation; a typical dimension of exposed crystals is 200 μm. However, the erosion mode in potassium feldspar is sensitive to the local conditions: it was observed on individual grains that part of the grain is eroded, whereas other parts of the same grain are untouched. An example is shown in Fig. 4c.

In the granite samples, feldspar and quartz are simultaneously eroded. The feldspar which is known to have cleavage planes was broken in a transcrystalline fashion; dimensions of the exposed crystals are

between 150 μm and 250 μm. The fracture occurred in steps with a typical step-width of 600 μm. The quartz showed a very brittle behaviour with smooth fracture planes; the fracture appeared also in the shape of individual elongated crystals with widths between 400 μm and 600 μm. This is illustrated in Fig. 5. Erosion sites in mica showed a platy morphology; single platelets seemed to be broken away through basal cleavage.

The limestone samples were eroded by two mechanisms. At low intensity coarse grain conglomerates with diameters between 800 μm and 1000 μm were exposed; an example is shown in Fig. 6a. At the rim of the major erosion crater (zone I) larger grains with up to 5 mm in diameter as visible in Fig. 6b and deep impressions between them could be observed. If intensity was increased, individual grains with an average diameter of 100 μm were exposed and removed, which is about two times the cleavage spacing of the calcite crystals.

The marble was eroded in a two-step mode. Individual calcite crystals with a dimension of about 800 μm were exposed at the surface. However, transcrystaline cleavage could also be observed in the calcite minerals; the size of the cleavage planes was typically 200 μm.

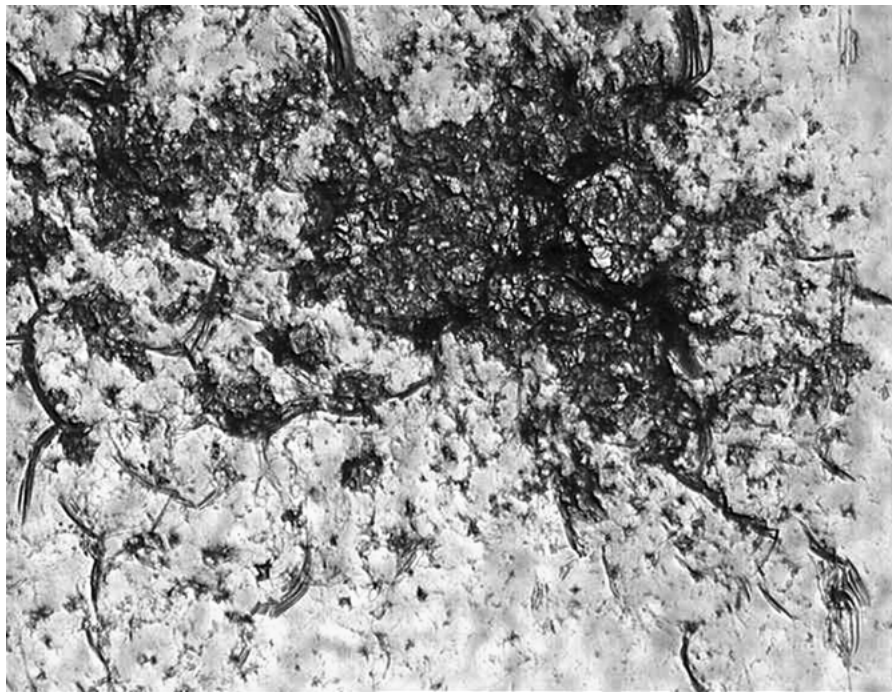

(a)

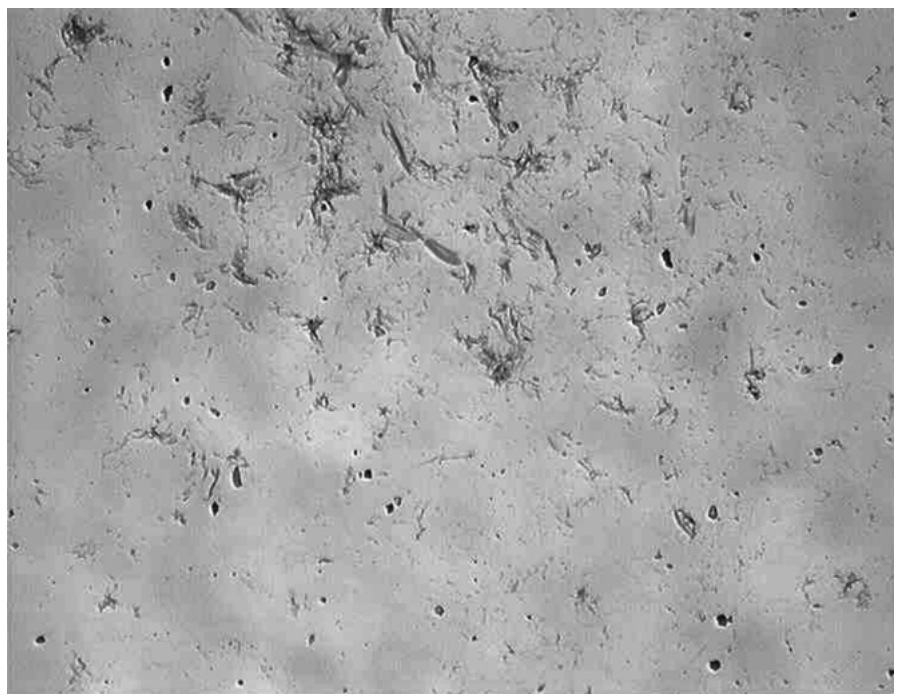

(b)

Figure 2 Glass sample eroded at $t_E = 60$ s. (a) Position: centre of zone I; image width: 11 mm, (b) Position: 2 mm away from centre of zone I; image width: 7 mm and (c) Position: zone II (2 mm away from zone I); image width: 2 mm. (*Continued*)

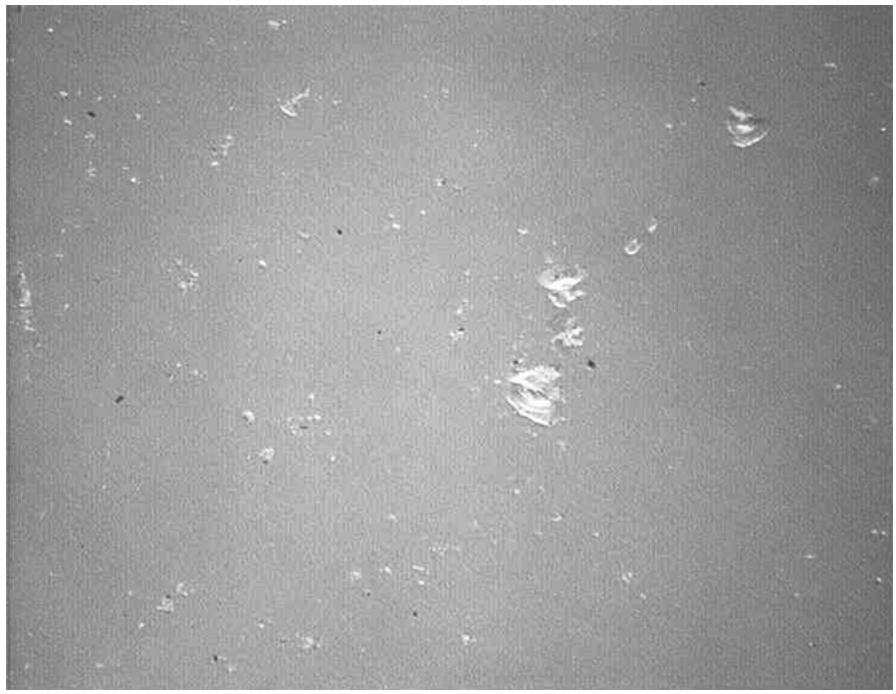

(c)

Figure 2 (*Continued*).

Figure 3 Pit formation in cement matrix and aggregate. Concrete 55; location: zone II (4 mm away from zone I); image width: 17 mm; $t_E = 5$ s.

The failure in schist was strongly localised. At pronounced specimen locations (zone I) deep grooves with widths up to 500 μm could be observed. Such grooves are shown in Fig. 7. Inside these grooves, the material failed by intergranular exposure of crystals with diameters between 100 μm and 150 μm.

3.3. Material resistance parameters

Fig. 8 shows the influence of the density on the cavitation erosion rate. A logarithmic scale is used at the ordinate because of the wide range of erosion data that covers six orders of magnitude. There is no distinct relationship between these two parameters. However, the two groups 'concrete' and 'rock material' can be distinguished. Whereas the conventional concrete mixtures are located in the upper centre region of the diagram, the rocks are concentrated in the right lower section. But there is also no general trend between the materials inside these two groups. Rocks with comparable densities (like granite and limestone) show dramatic differences in their erosion resistance (consider the logarithmic scale at the ordinate).

Fig. 9 shows the relationship between compressive strength and cavitation erosion rate. There is no general distinct trend between both parameters. Exceptions are the concrete mixtures 1, 2, 3 and 11 in the upper left region of the diagram: Here, cavitation erosion rate decreases as compressive strength increases. For the rock materials, in contrast, the scatter in data is dramatic. The rhyolite having the highest compressive strength shows the lowest cavitation erosion resistance among all rocks.

Fig. 10a shows the influence of the fracture toughness on the cavitation erosion rate. For comparison, results from cavitation erosion tests on ceramics reported in [22] are shown in Fig. 10b (note the logarithmic scale at the ordinate). Both relationships can reasonably be fitted by an exponential function:

$$R_E = c_1 \cdot K_{Ic}^{-n}. \tag{5}$$

The value for the power exponent is $n = 1.79$ for the ceramics. The exponent is $n = 2.93$ for the materials investigated in this study, but the coefficient of regression, $R^2 = 0.67$, is rather low. There is a very interesting feature in Fig. 10a: the glass and the high-strength silica cement do not fit into the regression. Their erosion

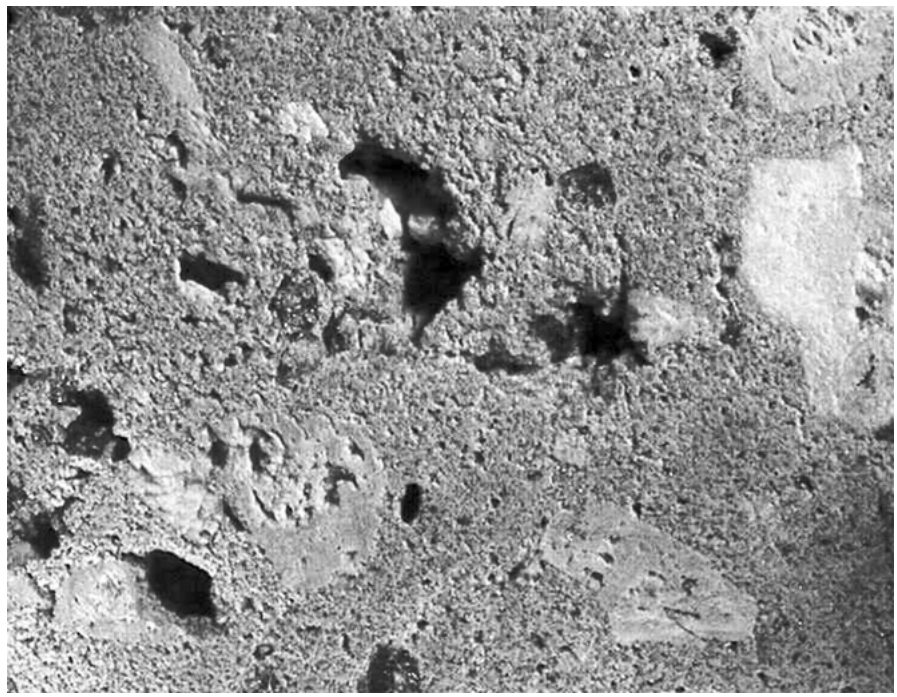

(a)

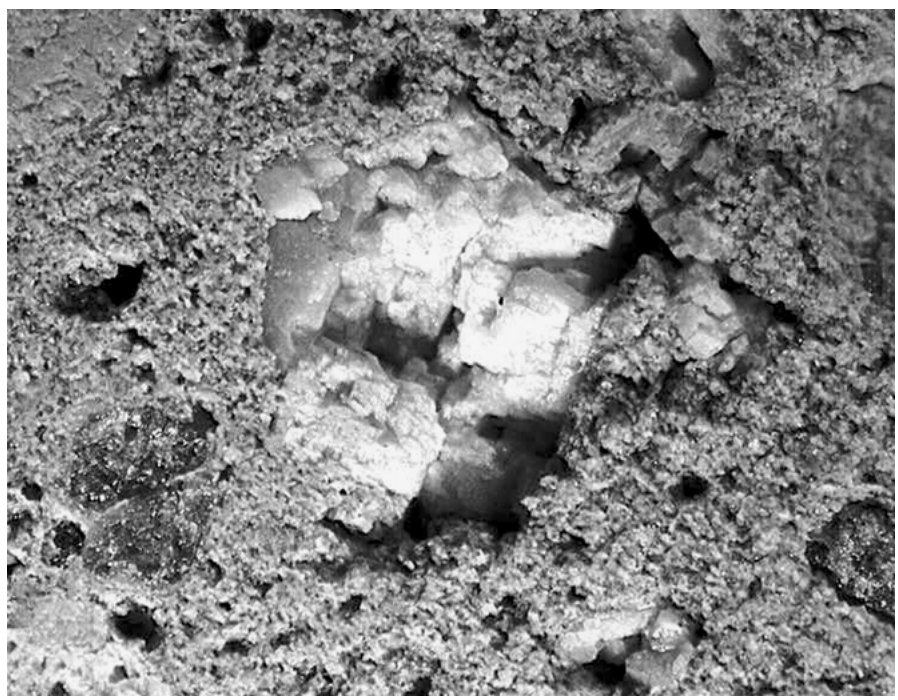

(b)

Figure 4 Erosion damage in rhyolite. (a) $t_E = 60$ s; image width: 17 mm, (b) $t_E = 120$ s; image width: 9 mm and (c) $t_E = 30$ s; image width: 5 mm. (*Continued*)

(c)

Figure 4 (*Continued*).

Figure 5 Fracture planes in quartz (granite); image width: 13 mm; $t_E = 180$ s.

resistance is much higher than expected by the exponential fit. These two materials own the highest brittleness values among the materials in this study, and can be considered as materials with a low degree of pores, flaws and pre-existing microcracks. The latter argument confirms observations in [23] and [24] where it was found that a high-strength low-porosity silica mortar has a cavitation erosion resistance 4 times and 16 times, respectively, higher than a conventional Portland cement mortar. It is very likely that the constant c_1 in Equation 5 depends on the structural homogeneity of the materials; it may decrease if bond between matrix and inclusions improves. The granite in Fig. 10a has also a rather high erosion resistance relative to the regression line. This result is in agreement with measurements reported in [7]. However, the explanation for the high resistance of the granite is the high degree of crack deflection and crack stopping. Detailed SEM-inspections of the erosion site showed a net of isolated microcracks that do not intersect [7]. If the glass and the silica cement are excluded from the regression, the power exponent increases up to $n = 3.44$ and the coefficient of regression increases to an acceptable level of $R^2 = 0.91$.

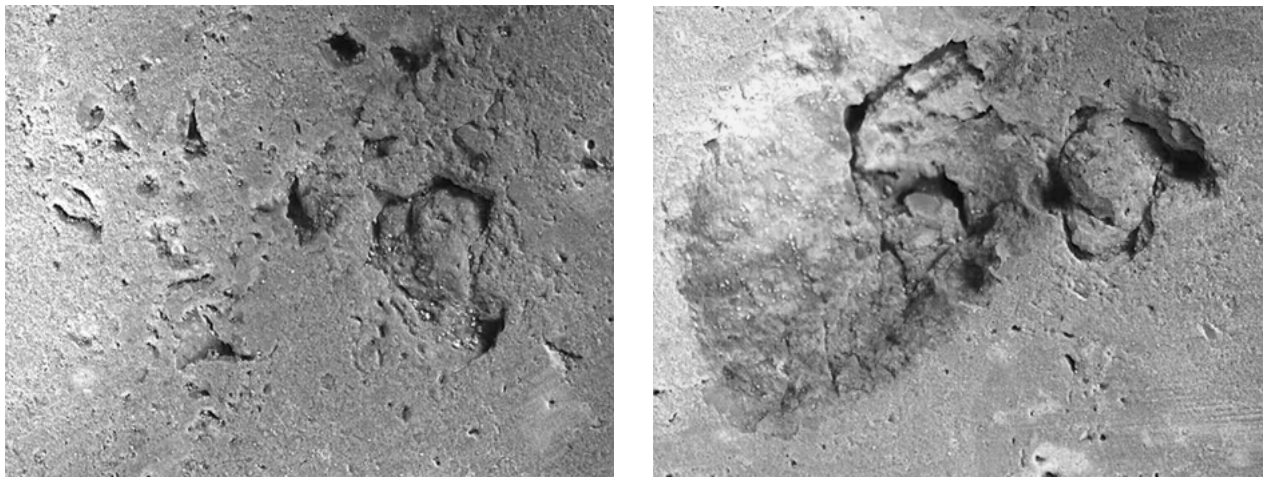

(a) (b)

Figure 6 Erosion damage in limestone; image width: 17 mm. (a) $t_E = 60$ s and (b) $t_E = 180$ s.

For materials eroded in a layer-to-layer mode predominantly by intergranular fracture, the erosion rate can be approximated by a model developed in [25]. Note from Fig. 11 that this assumption holds for certain materials investigated in this study. The model delivers:

$$V_E = c_2 \cdot N_G \cdot d_M^3 + \Psi_G. \tag{6}$$

In the equation, V_E is the volumetric erosion rate, N_G is the number of grains eroded per unit time, and d_M is the average grain size. The constant c_2 considers the grain shape, and the parameter Ψ_G takes into account a certain number of damaged individual grains. Further treatment of the problem delivers [25]:

$$V_E \propto \frac{d_M}{\gamma_M} + \Psi_M. \tag{7}$$

In the equation, γ_M is the specific surface energy of the material. Thus, erosion rate is linearly related to the material grain size and inversely related to the specific surface energy. The specific surface energy can be replaced by Irwin's crack extension force, $G_{Ic} = 2\gamma_M$. Also, the volumetric erosion rate can be replaced by R_E/ρ_M. Further treatment with standard equations from linear-elastic fracture mechanics delivers the following relationship:

$$R_E \propto \frac{d_M \cdot E_M \cdot \rho_M}{K_{Ic}^2} \propto \Phi. \tag{8}$$

Note that the power exponent of 2 for the fracture toughness is in good agreement with the power exponent resulting from Waldherr's [22] experimental results for ceramics ($n = 1.79$). However, the model can

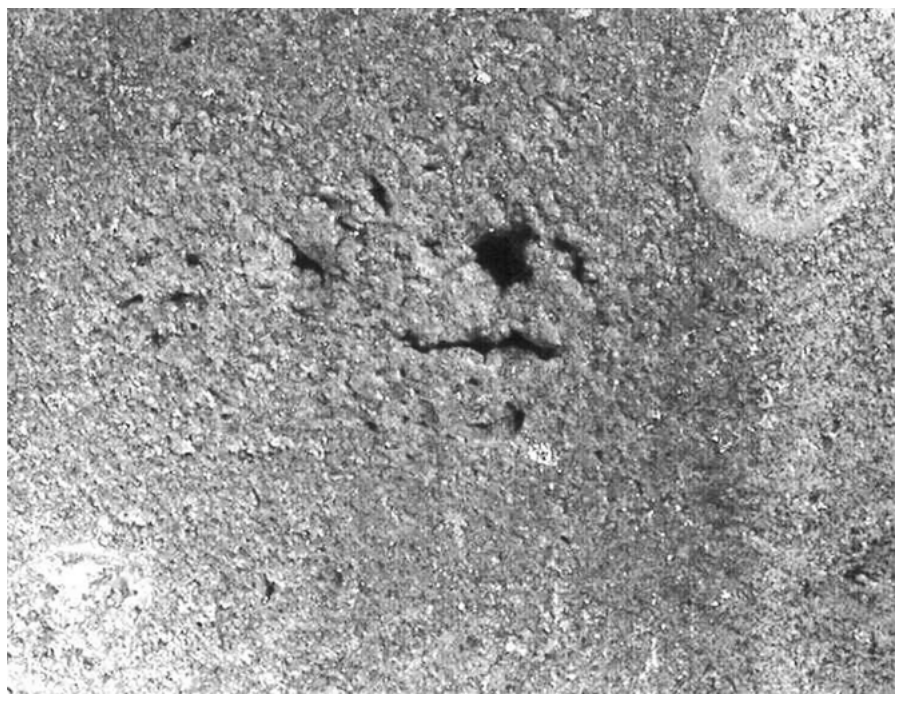

Figure 7 Erosion damage in schist; image width: 17 mm; $t_E = 180$ s.

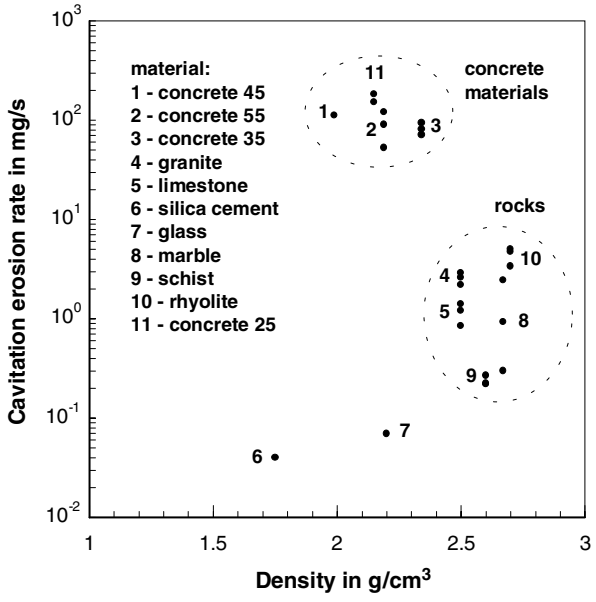

Figure 8 Relationship between target density and cavitation erosion rate.

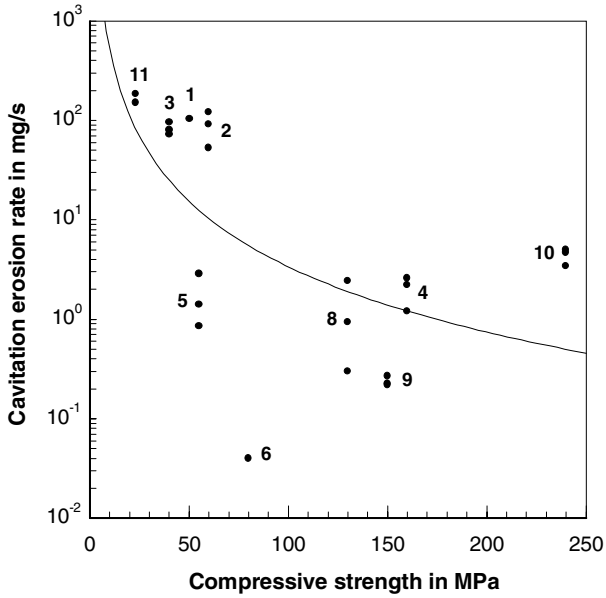

Figure 9 Relationship between compressive strength and cavitation erosion rate; numbers correspond to Fig. 8.

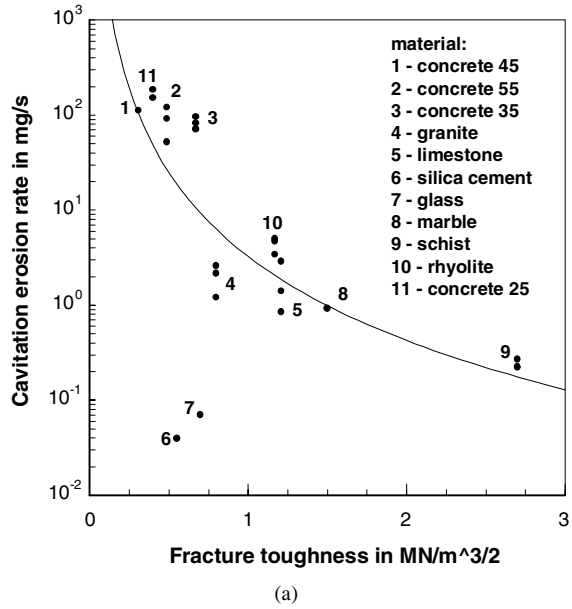

(a)

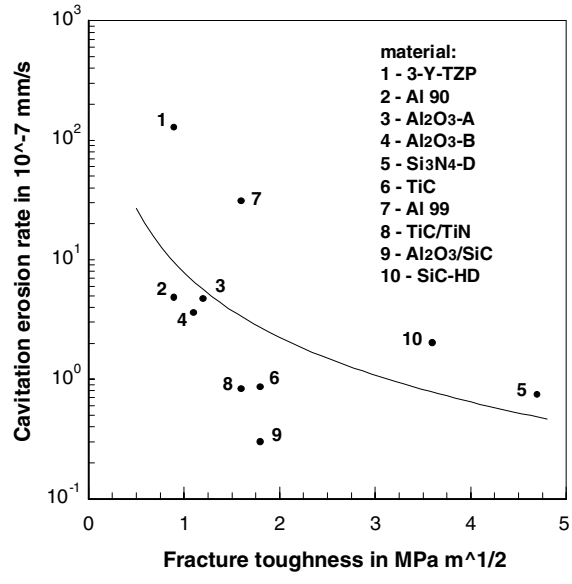

(b)

Figure 10 Relationship between fracture toughness and cavitation erosion rate. (a) Rocks, cementitious materials and glass and (b) ceramic materials [22].

not describe the cavitation erosion of the materials investigated in this study because of the power exponent of $n = 3.44$. Changes in the fracture toughness are more important for rocks than for ceramics. However, an intergranular layer-by-layer material removal as assumed for the derivation of Equation 8 was observed in most of the concrete materials. Examples are shown in Fig. 11. The parameter n is probably a function of the R-curve behavior, characterized by $K_{\mathrm{Ic}}^{*} = K_{\mathrm{Ic}} \cdot L^{\alpha}$, with L being crack length. For elastic materials: $\alpha = 0, n = 2$. For materials with R-curve behavior: $0 < \alpha \leq 0.5$, $n \to 3.44$. However, this issue needs further systematic study. The influence of the grain size, as expressed by Equation 8 is verified by the concrete materials. If fracture toughness, density and Young's modulus are of comparative magnitude, erosion resistance increases as aggregate size increases. The constant Φ in Equation 8 contains only material parameters and is, therefore, is a measure of the cavitation erosion resistance. The linear relationship between cavitation erosion rate and Φ as suggested by Equation 8 is verified in Fig. 12 for several materials. The scatter in the results for concrete 55 is most probably due to the different properties of matrix and aggregate. The low cavitation erosion rates for the silica-cement and the schist, which are materials with a very small grain size, further verify Equation 7.

For many metals, the linear elastic strain energy density shows a distinct linear relationship to the erosion resistance for cavitation erosion [26] and drop impact erosion [27]. The linear elastic strain energy density (for metals the term 'ultimate resilience' is sometimes used) is defined as follows:

$$E_{\mathrm{D}} = \frac{\sigma_{\mathrm{t}}^{2}}{2 \cdot E_{\mathrm{M}}} \tag{9}$$

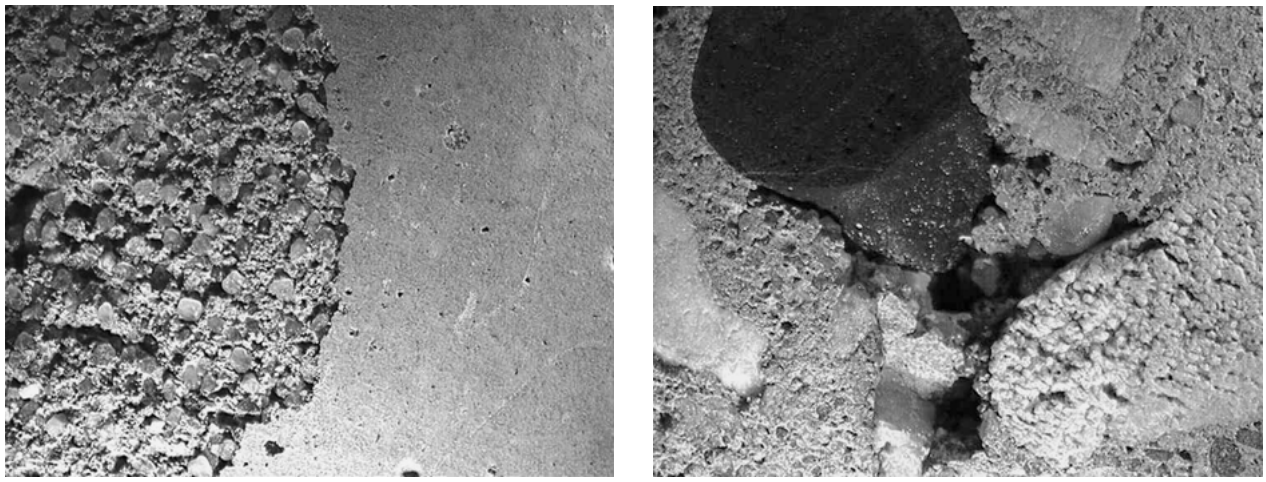

(a) (b)

Figure 11 Intergranular material removal modes in two materials. (a) Removal of cement layer from concrete 25 (image width: 17 mm; $t_E = 10$ s). (b) Integranular cracking between matrix and coarse inclusion in rhyolite (image width: 17 mm; $t_E = 60$ s).

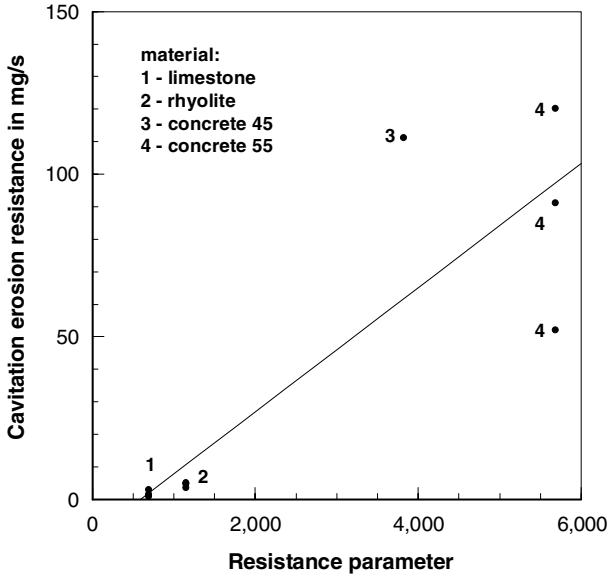

Figure 12 Relationship between Φ according to Equation 8 and cavitation erosion resistance.

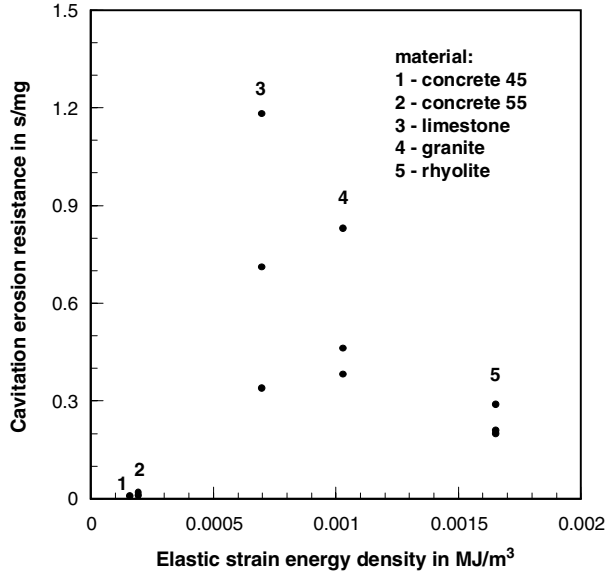

Figure 13 Relationship between elastic strain energy and cavitation erosion resistance.

Here, σ_t is the tensile strength and E_M is Young's modulus. The cavitation erosion resistance is the reverse of Equation 2. The relationship between linear elastic strain energy density and cavitation erosion resistance is shown in Fig. 13. There is no distinct trend between both parameters as reported for ductile metals. The materials considered in this study are tension-softening materials characterised by a considerable decreasing branch in the stress-strain curve after the ultimate stress. This type of material absorbs additional energy due to crack surface friction, crack bridging and microcrack formation [28]. It is shown for the erosion by high-speed water jets that this specific behaviour affects the erosion resistance [29]. Therefore, Equation 8 may be replaced by the true strain energy density [30]. This issue is an interesting topic for further investigation.

4. Summary

The results of this study can be summarised as follows.

- Short-time cavitation erosion of rocks and cement-based composites with exposure times as low as 5 seconds generates measurable damage. Therefore, cavitation erosion is a promising method to assist mechanical rock drilling.
- Mineral composition plays a major role in the cavitation erosion of the material. The erosion mainly occurs in an intergranular or intercrystalline mode, respectively.
- Fracture toughness of rock and conventional concrete is a good indication of cavitation erosion resistance. However, structural homogeneity (pores, interfaces, pre-existing flaws) is a second important evaluation parameter.
- A parameter $\Phi = d_M \cdot E_M \cdot \rho_M / K_{Ic}^n$ can be used to determine the cavitation erosion resistance of the materials.
- The cavitation erosion of the rock materials tested in this study is always higher than that of conventional concrete mixtures.

- Linear elastic strain energy density is not a measure of the cavitation erosion resistance for rocks and cementitious composites.

Acknowledgments

This investigation was funded by the German Research Foundation, Bonn, Germany, through a Habilitation fellowship. Thanks is addressed to Dr. Tai, Institute of Materials Science, Hanover University, for his help with the cavitation erosion tests, and to the Department of Mining, Metallurgy and Geosciences, Aachen University, for the specimen preparation and for the permission to use microscope facilities.

References

1. A. A RIBEIRO, L. V. DA CUNHA, D. P. DA SILVA and F. O LEMOS, in Proc. 9th Int. Congress on Large Dams, Istambul, 1967, Vol. 2, p. 315.
2. R. CLANCY, D. MARK and B. CHRISTOPHER, in 4th Int. Symp. on Cavitation, Pasadena, June 2001, p. 20–23.
3. F. A. ANGONA, *Int. J. Rock Mech. Min. Sci. & Geomech. Abstr.* **11** (1974) 115.
4. A. F. CONN and R. P. RADTKE, *The Oil and Gas J.* (1977) 129.
5. M. MAZURKIEWICZ and D. A. SUMMERS, in Proc. 6th Int. Symp. Jet Cutting Technology, edited by H. S. Stephens and E. B. Davies (BHRA, Cranfield, 1982) p. 27.
6. N. K. BOURNE, T. OBARA and J. E. FIELD, *Proc. Roy. Soc. London*, Ser. A **452** (1996) 1497.
7. F. ERDMANN-JESNITZER, H. LOUIS and WIEDEMEIER, in Proc. 4th Int. Symp. Jet Cutting Technol., edited by J. Clarke and H. S. Stephens (BHRA, Cranfield, 1978) p. 29.
8. A. W. MOMBER, *Wear* **241** (2000) 47.
9. F.G. HAMMITT, "Cavitation and Multiphase Flow Phenomena" (McGraw-Hill, New York, 1980).
10. W. H. ISAY, "Kavitation" (Schiffahrts-Verlag, Hamburg, 1989).
11. R. T. KNAPP, J. T. DAILY and F. H. HAMMITT, "Cavitation" (McGraw-Hill, New York, 1979).
12. W. LAUTERBORN and H. BOLLE, *J. Fluid Mech.* **72** (1975) 391.
13. J. P. DEAR and J. E. FIELD, *ibid.* **190** (1988) 409.
14. R. P. TONG, W. SCHIFFERS, S. J. SHAW, J. R. BLAKE and D. C. EMMONY, *ibid.* **380** (1999) 339.
15. Y. MURAKAMI, "Stress Intensity Handbook," Vol. 1 (Pergamon Press, Oxford, 1987) p. 13.
16. F. ERDMANN-JESNITZER and H. LOUIS, in "5. Sitzung Arbeitskreis Bruchvorgänge" (Deutscher Verband für Materialprüfung, Karlsruhe, 1973) p. 101.
17. M. S. PLESSET and R. B. CHAPMAN, *J. Fluid Mech.* **2** (1971) 283.
18. P. T. TAI, Personal communication, Institute of Materials Science, Hanover University, 2000.
19. J. E. FIELD, in "Tribology in Particulate Technology," edited by B. J. Briscoe and M. J. Adams (Adam Hilger, Bristol, 1987) p. 416.
20. N. K. BOURNE and J. E. FIELD, *J. Appl. Phys.* **78** (1995) 4423.
21. I. M. DANIELS and R. E. ROWLANDS, *Exper. Mechan.* (1975) 449.
22. E. U. WALDHERR, PhD thesis, Ruhr-University, Bochum, 1991.
23. C. M. PREECE and I. L. HANSSON, in Proc. 6th Int. Conf on Erosion by Liquid and Solid Impact, edited by J. E. Field (Cavendish Laboratory, Cambridge, UK, 1986) p. 3/1.
24. B. LIN, G. SHAN and Y. CAI, in Proc. 3rd CANMET/ACI Conf. on High-Performance Concrete, Kuala Lumpur, 1997, p. 485.
25. W. J. TOMLINSON, N. NALITSOUNAKIS and G. VEKINIS, *Ceramics Int.* **25** (1999) 331.
26. A. THIRUVENGADAM, in "ASTM STP 403" (ASTM, Philadelphia, 1967), p. 22.
27. F. J. HEYMANN, in "ASTM STP 474" (ASTM, Philadelphia, 1970) p. 212.
28. P. S. SHAH and C. OUYANG, *ASME J. Engng. Mater. and Technol.* **115** (1993) 300.
29. A. W. MOMBER, *Int. J. Fracture* **112** (2001) 99.
30. G. C. SIH and E. E. GDOUTOS, "Mechanics and Physics of Energy Density" (Kluwer Acad. Publ., Dordrecht, 1992).

Received 1 March
and accepted 24 September 2002